Journal of Power Sources 558 (2023) 232556

Contents lists available at ScienceDirect

Journal of Power Sources

journal homepage: www.elsevier.com/locate/jpowsour

Experimental study and modeling of water transport through short-side-chain perfluorosulfonic acid membranes

Amedeo Grimaldi [a], Andrea Baricci [a], Stefano De Antonellis [a], Claudio Oldani [b], Andrea Casalegno [a,*]

[a] Politecnico di Milano, Department of Energy, Via Lambruschini 4, 20156, Milano, Italy
[b] Solvay Specialty Polymers SpA, R&D Centre, Viale Lombardia 20, 20021, Bollate, Italy

HIGHLIGHTS

- Experimental characterization of dynamic water transport across PFSA membranes.
- New correlations for the dynamic water transport model of SSC membranes.
- Combination of dynamic vapour sorption and water permeation measurements.
- Effect of equivalent weight and porous layer treatment on water permeation.
- Identification of individual contributions to overall water permeation.

GRAPHICAL ABSTRACT

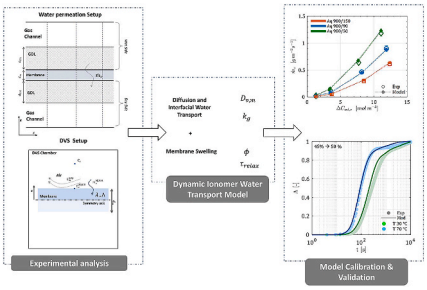

ARTICLE INFO

Keywords:
PEMFC
Short-side-chain ionomer
Membrane
Dynamic model
Polymer swelling
Water transport

ABSTRACT

Perfluorosulfonic acid polymer membranes are state-of-the-art electrolytes in PEMFCs and PEMWEs, and their degradation represents still one of the limiting factor to increase lifetime of electrochemical devices. Due to significant role of water in stressing degradation mechanisms, this work, through an experimental and theoretical analysis, deepens comprehension of materials and constructive properties of short-side-chain (SSC) membranes on dynamic water transport. A systematic analysis is carried out by analysing samples with different membrane thickness and *EW*, coupled with different gas diffusion layers. A model was adopted to analyse both steady-state and transient water transport tests, evaluating individual contributions to the total water mass transfer. Particular attention was given to swelling/shrinking mechanism, highlighting its strong impact on water sorption and membrane hydration. Membrane diffusion and interfacial mass transfer were independently investigated, identifying their interconnections with material-bulk and superficial properties. Results highlight that membrane with low *EW* (790 g mol^{-1}), coupled with hydrophilic gas diffusion layers that oppose negligible interfacial resistances to water transport, allows to reduce total resistance by approximately 39% compared to reference configuration (980 g mol^{-1}, hydrophobic).

* Corresponding author.
E-mail address: andrea.casalegno@polimi.it (A. Casalegno).

https://doi.org/10.1016/j.jpowsour.2022.232556
Received 21 October 2022; Received in revised form 6 December 2022; Accepted 18 December 2022
Available online 6 January 2023

1. Introduction

Perfluorosulfonic acid (PFSA) ionomers are multifunctional materials that are used for several applications in electrochemical devices, as polymer electrolyte membrane fuel cells (PEMFCs) and polymer electrolyte membrane water electrolyzers (PEMWEs) [1] with low [2] and platinum group metal (PGM) free electrodes [3]. PFSA ionomer constitutes the ion-conducting phase [4] in both the membrane and the catalyst layers (CLs) and it has a fundamental role on performance and durability [5]. Indeed, ionomer degradation is one of the major concerns for applications that require long lifetime, like stationary and heavy duty transport [6], and it is known to proceed by two mechanisms that deteriorate ionomer properties by chemical decomposition [7,8] and mechanical stresses [9]. In both cases, ageing is enhanced by specific operating conditions, especially *RH* cycling, but both the above-mentioned elements are strictly related to water transport and hydration [10]. This becomes particularly critical [11] considering the tendency of ionomer to swell/shrink when it gets hydrated/dehydrated, thus adding another element of complexity to understand water and ion transport mechanisms. While the correlation between mechanical stresses and ionomer durability is obtaining more and more attention, as demonstrated by recent literature [12–14], the role of the polymer swelling has not been thoroughly investigated. In particular, it is important to improve the knowledge on the relation between swelling mechanism and the effective transport properties under dynamic conditions.

Several PFSA ionomer chemistries were investigated and patented, starting from Nafion®, while other polymers were later commercialized, presenting the main differences in the lateral chain that includes the ion conducting sulfonic group [2]. In recent times, PFSA ionomers with short-side-chain (SSC) chemistries have gained particular attention because of their increased ionic conductivity and oxygen permeability [10,15]. To the best of our knowledge, there is huge literature about Nafion membrane properties on water transport, that are reviewed in the following lines, but no works in literature adopts a systematic approach to investigate the effect of SSC PFSA membrane properties [16], particularly equivalent weight (*EW*), on dynamic water transport. Thus, in this work our focus is devoted to understand dynamic water transport mechanisms under a wide range of operating conditions through SSC ionomers. Water uptake features of PFSA ionomers were characterized over the past few decades, using several experimental methods [4], among which dynamic water sorption (DVS) [17] and steady state water permeability tests (WPT) [18] are well-established techniques. Steady-state permeation tests can be divided into three categories, i.e. vapour-to-vapour permeation (VVP), liquid-to-vapour permeation (LVP) or liquid to liquid permeation (LLP) [16]. In this work the experimental methodology combines VVP/LVP and DVS measurements in order to wholly cover the operating conditions of PEMFCs and electrolyzers, under low humidity and flooded conditions.

Several works adopted LVP and VVP to measure the water diffusion coefficient in Nafion based membranes, with different experimental setups and assembly methods. Ge et al. [19] applied measurements of water permeation on Nafion membranes and determined that water transport includes adsorption/desorption at membrane/gas interface and adsorbed water diffusion through membrane, providing empirical correlations for interfacial mass-transfer coefficients. Majsztrik et al. [18] investigated water permeation across Nafion membranes with different thicknesses, evaluating the effect of vapour or liquid feeding on the global permeation coefficient. Adopting a similar methodology, other researchers measured water diffusion for other types of membranes [20–23]. As a general statement, values of steady-state diffusivity reported in the literature for Nafion membranes lie within the same order-of-magnitude (10^{-9} to 10^{-10} m^2 s^{-1}) [24].

Dynamic water uptake measurements have been performed by DVS to characterize Nafion based membranes [25,26]. Kusoglu and Weber [27] conducted differential DVS experiments on Nafion membranes and, by modelling water transport through the Fick's second law, observed that diffusion coefficient of water decreases with increasing relative humidity, reaching its lowest value (10^{-13} m^2 s^{-1}) under saturated vapour. Satterfield et al. [17] analysed water sorption and desorption on Nafion membranes observing a non-Fickian behaviour of DVS mechanism due to polymer swelling/shrinking. Differences in water uptake rates during adsorption and desorption were a debated theme over the years. The different rates were linked to the shape and hysteresis of sorption isotherm [28], to interfacial effects [19,29] and to the different structural reorganization of ionomer and water domains [26,30,31], as a consequence of polymer swelling/shrinking.

The literature analysis highlights that a more accurate physical description of all the involved mass-transport resistances in the process is required to deal with the complexity of water transport process across PFSA membranes, occurring at different length and time scales. The scope of the research is to improve the understanding of the mechanisms underlying water transport through PFSA membranes. The developed methodology is based on a proper combination of VVP and DVS tests and is applied to SSC ionomers. In particular, from VVP tests, water diffusion and interfacial mass transfer were investigated, whereas, from DVS, transient effects were analysed, with main focus on dynamics related to polymer swelling. Based on the aforementioned tests, through the fitting of six specific parameters, a complete water transport model, through ad-hoc semi-empirical correlations, is developed and used to describe properly the overall process.

2. Materials & methods

2.1. Research methodology

PFSA membranes, used in the following analysis, range over different values of thicknesses, from 50 to 150 μm and *EW*, from 790 to 980 g mol^{-1}, realized both by extrusion and casting technique from Aquivion® ionomer, as shown in Table 1. Membranes are labelled according to the following indications: commercial polymer name, nominal *EW*, nominal thickness. The four membranes based on Aquivion 980 and 870 were fabricated by extrusion and the one based on Aquivion 790 was prepared by casting technique. Membrane preparation technique was reported in a previous work [32]. Measured thickness of membranes can differ from the nominal one at most by 5 μm. In addition, a commercial Nafion® N-212 membrane, labelled as Nafion 1100/50, was tested as benchmark. Besides membranes, also different gas diffusion layers (GDLs) were investigated in water permeation tests. Commercial materials, namely Freudenberg H23I2 (uncompressed thickness: 222 μm) and Freudenberg H23 (uncompressed thickness: 210 μm), were used as gas diffusion layers in membrane assembly. The two GDLs, used in this work, have no micro-porous layer coating and they significantly differ in the fiber treatment. More precisely, PTFE is added in H23I2, which becomes hydrophobic, while it is absent in H23, which remains slightly hydrophilic [33]. Prior to testing, all membrane samples have undergone a standard pre-treatment procedure, regenerating each sample in deionized boiling water for 30 min, in order to remove all the impurities and to guarantee repeatability of measurements [4].

Table 1
Membrane tested under steady-state permeation and DVS tests.

Membrane name	Nominal Thickness d_m	Nominal Equivalent Weight *EW*
	[μm]	[$g\ mol^{-1}$]
Aquivion 980/50	50	980
Aquivion 980/90	90	980
Aquivion 980/150	150	980
Aquivion 870/50	50	870
Aquivion 790/50	50	790
Nafion 1100/50	50	1100

2.2. Experimental setup and procedures

2.2.1. Vapour-to-vapour permeation test

Water permeation across membrane is evaluated through VVP test. Samples are assembled between two gas diffusion layers, constituting a membrane assembly. The assembly is positioned between two flow field plates and pressed together by two aluminium blocks, as the experimental set-up presented in Ref. [34]. Sample area exposed to water permeation is equal to 7.7 cm^2. As visible in Fig. 1(a), the permeation cell is placed in order to have a high-humidity air stream, $\dot{V}^{w}_{air}$, referred as wet side, and a dry air stream, $\dot{V}^{d}_{air}$, referred as dry side, in a co-flow arrangement. At the outlet of wet and dry side, total pressure, temperature and relative humidity of the streams were recorded. The protocol was developed to test membranes under a set of defined operating conditions.

The total permeated water flux rate, $\dot{m}_v$, is computed according to Eq. (1), as shown in Ref. [35], assuming isothermal conditions, inlet air on dry side completely dry and negligible air permeation across membrane. $RH^{d,out}$ and p_{tot} are relative humidity and pressure of the stream on dry side outlet.

$$\dot{m}_v = \frac{MM_{H_2O}}{MM_{air}} \frac{RH^{d,out}}{\frac{p_{tot}}{p_{vsat}} - RH^{d,out}} \frac{\dot{M}^{d}_{air}}{A_{cell}} \tag{1}$$

The total resistance $R_{tot,v}$, reported in Eq. (2), can be expressed as the ratio of the gas phase concentration difference across membrane and the molar water permeated flux.

$$R_{tot,v} = \frac{\Delta C_{ml,v}}{\frac{\dot{m}_v}{MM_{H_2O}}} \tag{2}$$

In Eq. (2), the logarithmic mean water concentration, $\Delta C_{ml,v}$, evaluated as shown in Eq. (3), represents the effective driving force for water transport across the membrane, as proposed in Ref. [21], taking into account the change of water concentration along wet and dry channel because of water permeation through the membrane.

$$\Delta C_{ml,v} = \frac{\left(C_v^{d,in} - C_v^{w,in}\right) - \left(C_v^{d,out} - C_v^{w,out}\right)}{ln\left(\frac{C_v^{d,in} - C_v^{w,in}}{C_v^{d,out} - C_v^{w,out}}\right)} \tag{3}$$

The combined standard uncertainty was estimated according to standards [36] and reported in figures in Section 3.

2.2.2. Dynamic vapour sorption

Water sorption tests are performed using an automated, gravimetric, dynamic vapour sorption (DVS) analyser (namely AQUADYNE DVS™ 2 by Quantachrome Instruments). Experimental uncertainty of measured quantities are the following: temperature - ± 0.2 °C; relative humidity – from ±0.8% at 20 °C to ±1.8% at 70 °C; weight - ± 1.0 μg plus 0.001%

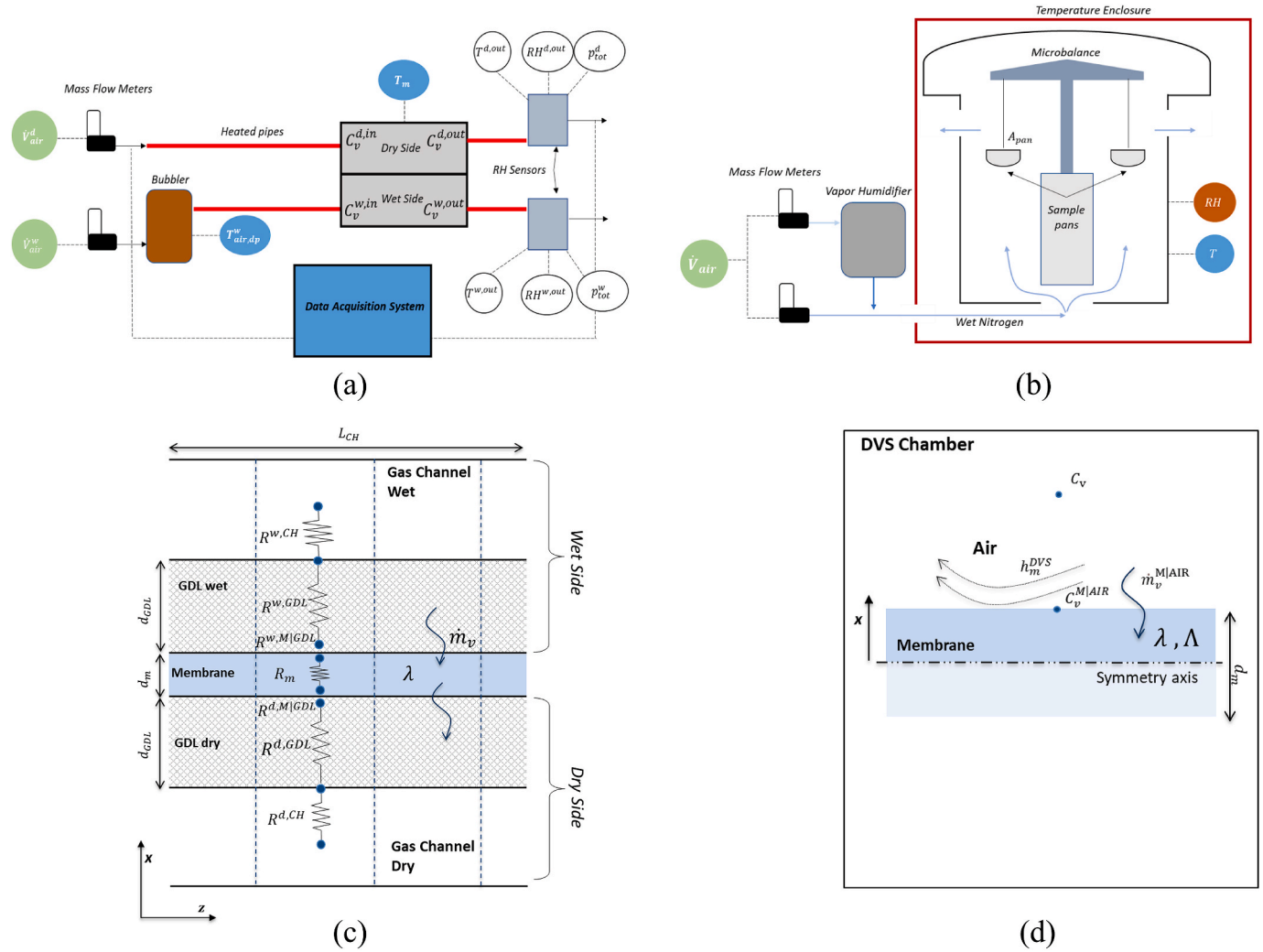

Fig. 1. (a) Layout scheme of permeation test apparatus for VVP. (b) Layout scheme of DVS apparatus. (c) Scheme of the membrane assembly, with indication of individual contributions to overall mass transport. (d) Model framework for DVS tests.

of suspended mass. Each membrane sample is placed over the balance plate of the gravimetric analyser, as visible in scheme reported in Fig. 1 (b). Once the drying step is completed at 80 °C in a nitrogen atmosphere at ambient pressure, to obtain the reference anhydrous mass, $m_{m,a}$, the samples are subject to increasing humidity conditions from 0% to 90% *RH* and, subsequently, to decreasing humidity conditions, from 90% to 0%, with 5% intervals, at a given temperature. The DVS instrument measures mass change over time and tests are performed at different temperatures: 30 °C, 50 °C and 70 °C respectively. In Eq. (4), the membrane water content λ is computed for each sample by knowing the dynamic mass measurement, m_m, and the mass of the dry ionomer, $m_{m,a}$.

$$\lambda = \frac{n_{H_2O}}{n_{SO_3^-}} = \frac{m_m - m_{m,a}}{m_{m,a}} \frac{EW}{MM_{H_2O}} \tag{4}$$

Data from the adsorption apparatus are collected in continuum to yield the curves of dynamic vapour sorption as function of time; the final datapoint of each *RH* step is used to draw the equilibrium isotherm adsorption curve as function of relative humidity. The determination of water transport properties from a DVS on a membrane involves a careful examination of all the phenomena and parameters driving water uptake and transport through the membrane sample [4]. Both VVP and DVS tests are later labelled according to the following indication: test type, membrane temperature. Further information on experimental procedure is reported in Section SI-1 of Supplementary Information (SI).

2.3. Model description

In this section, a 1D+1D model of the membrane assembly is presented and discussed. According to Fig. 1(c), the control volume includes the ionomer, the GDLs and the wet and dry air channels. The following assumptions have been adopted: isothermal conditions; water diffusion occurring only through ionomer thickness (negligible planar diffusion); water in vapour phase in all domain volumes other than membrane; no vapour accumulation in air channels and GDLs. Governing equations are reported in sections 2.3.1, 2.3.2 and 2.3.3 respectively for ionomer, GDL and air channel domains. Finally, it is explained how the model is used to interpret steady-state VVP and transient DVS measurements in section 2.3.4.

2.3.1. Ionomer water transport

Molecular diffusion flux of water through ionomer is driven by the gradient in chemical potential of water [4] and proportional to the chemical diffusivity. An alternative approach in the literature [29] links the diffusion flux to the gradient in water concentration, which is directly linked to the water content, λ. A consistency is required between the two models in order to guarantee the physical basis, as discussed in Ref. [37], which relies on the definition of the Darken factor. In Eq. (5), the conservation equation of λ is reported, where $D_{v,m}$ is the effective Fickian diffusion coefficient of water through the ionomer.

$$\frac{\partial \lambda}{\partial t} = \frac{\partial}{\partial x}\left(D_{v,m}\frac{\partial \lambda}{\partial x}\right) \tag{5}$$

From literature [38], it is possible to find different mathematical forms describing the non-linear nature of the Fickian diffusivity coefficient $D_{v,m}$ with respect to the local water content λ, as correlations proposed by Springer et al. [39] and, later, by Kulikovsky [40]. The correlation derived by Olesen [41] on data from Nafion [20], reported in Eq. (6), and later modified by Liso et al. [22], is adopted in the following study.

$$D_{v,m} = \xi_{mb}\left(1 + \frac{\overline{V}_{H_2O}}{\overline{V}_m}\lambda\right)^{n_m}\left(1.0 + 2.7\times 10^{-3}\lambda^2\right)\left[1 + \tanh\left(\frac{\lambda - \lambda_{tp}}{\delta_{tp}}\right)\right]\exp\left(-\frac{E^m_{act}}{\mathscr{R}T}\right) \tag{6}$$

where $\overline{V}_{H_2O}$ and $\overline{V}_m$ are the molar volume of liquid water and of dry membrane ionomer, assumed respectively equal to 1.8×10^{-5} m^3 mol^{-1} and to EW/ρ_m. It should be noted that the diffusivity correlation, expressed in Eq. (6), is determined from the chemical diffusivity and the Darken factor for different membrane hydration conditions on Nafion membranes [22]. The Darken factor could be explicitly used in the correlation for estimating the Fickian diffusivity. However, in the investigated conditions, such parameter depends on the isotherm fitting model and, therefore, it was preferred to keep the form of the correlation of Eq. (6) already adopted in the literature. Moreover, the presence of the term, $(1 + \overline{V}_{H_2O}/\overline{V}_m\lambda)$, in Eq. (6), is associated to swelling of membrane and the parameter n_m varies according to the preferential directions of polymer deformation. In this work, n_m is assumed equal to −2, according to literature [22]. Finally, δ_{tp} and E^m_{act} are taken from literature: the former for the low sensitivity, the latter for its low uncertainty in literature [22].

Testing of materials other than Nafion allows the tuning of the two characteristic parameters, present in Eq. (6), namely ξ_{mb}, λ_{tp}. Interfacial water transport occurring at the ionomer/gas boundary, can be modelled by Eq. (7), where k_g is the interfacial mass transport coefficient, function of temperature and water content, λ, through Eq. (8) [19]. The driving force is the difference between the actual value of λ and λ^*, that is the quasi-equilibrium value for water content in the ionomer.

$$\dot{m}_v^{M|GDL} = k_g\frac{\rho_m}{EW}MM_{H_2O}(\lambda^* - \lambda) \tag{7}$$

$$k_g = \xi_{ad}\,\lambda^{1.6}\exp\left[\frac{E^k_{act}}{\mathscr{R}}\left(\frac{1}{303} - \frac{1}{T}\right)\right] \tag{8}$$

Different mechanic models are present in literature trying to describe stress relaxation of ionomer [42] at microscopic level, but it is out of the scope of this work. An effective swelling model, capturing the effect of membrane swelling on water transport, is reported in Ref. [43] and adapted for computing λ^*, as defined in Eq. (9).

$$\lambda^* = (1 - \varphi)\lambda_{eq} + s_{relax} \tag{9}$$

where φ represents the fraction of volume available for water uptake as polymer relaxes over time and s_{relax} denotes, instead, a variable that accounts for the dynamics of stress relaxation through Eq. (10).

$$\frac{ds_{relax}}{dt} = -\frac{1}{\tau_{relax}}\left(s_{relax} - \varphi\lambda_{eq}\right) \tag{10}$$

The equilibrium water content, λ_{eq}, is function of water activity and temperature and is described by the sorption isotherm. Experimental data for sorption isotherms are directly used in the model. To better investigate sorption isotherm of the different materials, the Dubinin–Astakhov (DA) model [44] was used, expressing λ_{eq} as function of the adsorption potential, *A*.

$$\lambda_{eq} = \lambda^0_{eq}\exp\left(-\frac{A}{E_{DA}}\right)^{\eta} \tag{11}$$

where η is a fitting parameter proposed by Dubinin and Astakhov, *A* is the adsorption potential, and E_{DA} is the characteristic energy of adsorption of the given system. The adsorption potential *A* is evaluated from *T* and *RH*.

$$A = -\mathscr{R}T\,ln(RH) \tag{12}$$

2.3.2. GDL vapour transport

Water vapour diffusion through porous medium, adjacent to gas channels, is governed by the following equations.

$$\frac{d}{dx}\left(D_{v,GDL}\frac{dC_v}{dx}\right) = 0 \tag{13}$$

$$D_{v,GDL} = \varepsilon\left(\frac{\varepsilon - \varepsilon_{pc}}{1-\varepsilon_{pc}}\right)^{n_e} \frac{1}{\frac{y_{O_2}}{D_{H_2O\ O_2}} + \frac{y_{N_2}}{D_{H_2O\ N_2}}} \tag{14}$$

Where ε is the compressed layer porosity, $D_{v,GDL}$ is the effective diffusivity, y_{O_2} and y_{N_2} are the molar fractions of oxygen and nitrogen, ε_{pc} is the percolation threshold [45]. The binary diffusion coefficients, $D_{H_2O\ O_2}$ and $D_{H_2O\ N_2}$, were calculated exploiting the Fuller method [46].

2.3.3. Gas channels vapour transport and boundary conditions

Conservation equations for mass fluxes, inside channel volumes, are solved for water vapour along channel direction.

$$\frac{d\dot{m}_v}{dz} = -\frac{\dot{m}_v^{\mathrm{GDL|CH}}}{L_{CH}} \tag{15}$$

$$\frac{dp_{tot}}{dz} = -\frac{f\mu}{2\,d_h^2}\frac{\dot{m}_{tot}}{\frac{h_{CH}}{L_{CH}}\frac{p_{tot}}{\mathscr{R}T}MM_{air}} \tag{16}$$

where $\dot{m}_v$, $\dot{m}_v^{\mathrm{GDL|CH}}$ are the mass flux along channel direction and mass flux at GDL/channel interface of water vapour, whereas $\dot{m}_{tot}$, p_{tot} are the mass flux and pressure in gas channels and f is the friction factor, computed according to Ref. [47].

$$\dot{m}_v^{\mathrm{GDL|CH}} = h_m\, MM_{H_2O}\left(C_v - C_v^{GDL|CH}\right) \tag{17}$$

The convective transport resistance at the GDL|CH interface is included in the model, trough Eq. (17), and determined by the convective mass transport coefficient, h_m, function of Sherwood number, Sh. A specific correlation, reported in Eq. (18) and defined as a function of the hydraulic diameter (d_h), Reynolds (Re) and Schmidt (Sc) numbers, for estimating Sh is used [48]. The hydraulic diameter was evaluated accordingly to Eq. (19).

$$Sh = 1.62\left(\frac{d_h}{L_{CH}}Re\,Sc\right)^{0.33} \tag{18}$$

$$d_h = \frac{2\,w_{CH}h_{CH}}{w_{CH}+h_{CH}} \tag{19}$$

Molar fluxes of species entering wet and dry channels are set equal to the experimental value for the different operating conditions.

2.3.4. Numerical implementation and solution

The model is used to analyse vapour to vapour permeation and dynamic vapour sorption tests. In VVP tests, vapour flow across membrane assembly is measured in steady state conditions. Equations of ionomer water transport, GDL vapour transport and channels gas transport are solved together, with appropriate boundary conditions adopted in tests, namely overall temperature, airflows relative humidity and flowrates. Pressure is set at the outlet of channel volumes equal to atmospheric pressure, consistently with experimental values. In addition, transient terms of Eqs. (5) and (10) are set equal to zero.

Instead, in DVS tests only ionomer water mass transfer, occurring only through membrane thickness, is evaluated: domain consists of ionomer sample exposed to airflow at both sides, without any GDLs and channels, as shown in Fig. 1(d). Therefore, the dynamic governing equations of water transport in the ionomer, Eqs. (5)–(12) and (17), are directly coupled with boundary conditions used in the related tests. More precisely, in Eqs. (7) and (17) the water flow rate is evaluated at the membrane - air interface ($\dot{m}_v^{\mathrm{M|AIR}}$ instead of $\dot{m}_v^{\mathrm{GDL|CH}}$), and in Eq. (17) the same adaptation is done for the vapour concentration ($C_v^{M|AIR}$ instead of $C_v^{GDL|CH}$), as shown in Fig. 1(d). Moreover, because of symmetry conditions in the problem, since membrane sample is exposed to chamber air on both sides, it is possible to solve the governing equations considering a domain size equal to half of membrane thickness d_m and assuming no vapour flux in the middle of the sample. The convective mass transfer coefficient h_m^{DVS} of Eq. (17) is estimated experimentally. Evolution in time of vapour concentration, C_v, in chamber is extrapolated from the experimental data and used as boundary condition. In the following lines, according to forementioned considerations, governing equations used to analyse vapour to vapour permeation and dynamic vapour sorption tests are respectively referred as VVP and DVS models. In both cases, the set of equations is solved through Matlab software, using built-in routines.

3. Results & discussion

In this section, experimental and numerical results are shown and discussed. Firstly, sorption capacity at equilibrium is evaluated for the investigated membranes and an adequate modelling is proposed. Secondly, experimental results obtained for two reference membranes, namely Aquivion 980/50 and 980/150 are reported and discussed. Data are used to properly calibrate the DVS and VVP models introduced in Section 2. Finally, measured data of remaining membranes (Aquivion 980/90, 790/50 and 870/50) assembled with different GDLs are shown in combination with ones calculated through the calibrated model.

3.1. Adsorption isotherms of membranes

Water uptake behaviour of membranes was investigated using sorption isotherms that correlate equilibrium water content, λ_{eq}, with relative humidity, RH, at constant temperature. In Fig. 2(a), sorption isotherms of membranes with different EW are shown. Profiles denote a slight increase of water content slope for RH higher than 70%. According to Ref. [4], two regions can be evidenced: a low-RH region where water molecules form the first solvation shells around the ionic groups and a high-RH region, where water molecules are weakly bound or unbound to the former shells inside the hydrophilic domains. In addition, it is worth to note that λ_{eq} profiles show similar trends, indicating that in case of low EW the higher uptake of water is compensated by the higher number of sulfonic acid groups, in accordance with literature [49]. Obtained results are consistent with ones available in literature on SSC materials [50] for similar test conditions. Anyway, a previous research [51] highlights that in case of adsorption from liquid water, the lower EW, the higher λ. This effect was not observed in performed tests because membrane adsorption capacity was evaluated in wet air, with relative humidity lower than 90%.

In Fig. 2(b), the equilibrium water content is shown as a function of the adsorption potential of the Dubinin-Astakhov model. Results deal with all investigated membranes and are obtained at different temperatures. A minor deviation is observable among membranes with different thickness, comparable to one of literature data [52].

3.2. Reference membranes: experimental analysis and model calibration

3.2.1. Dynamic water uptake

Transient water uptake during vapour adsorption and desorption for membrane 980/50 is analysed. In Fig. 3, profiles for selected step-changes in humidity during a dynamic test are reported. Data are normalized according to Eq. (20), where $\lambda_{\min}$ and $\lambda_{\max}$ are the initial and final (at equilibrium) values of λ, given at a certain step in RH.

$$\Lambda = \frac{\lambda - \lambda_{min}}{\lambda_{max} - \lambda_{min}} \tag{20}$$

Two distinct phenomena, with significantly different time constants, are highlighted from DVS tests, both during adsorption (Fig. 3(a) and (b)) and desorption (Fig. 3(c) and (d)). For the same step in RH, the higher the temperature, the faster the water sorption or desorption. At initial times, the rate-limiting mechanism is the superficial mass transport, which can be associated to the external convection over membrane sample and to interfacial transport [17]. Further insight on this aspect is

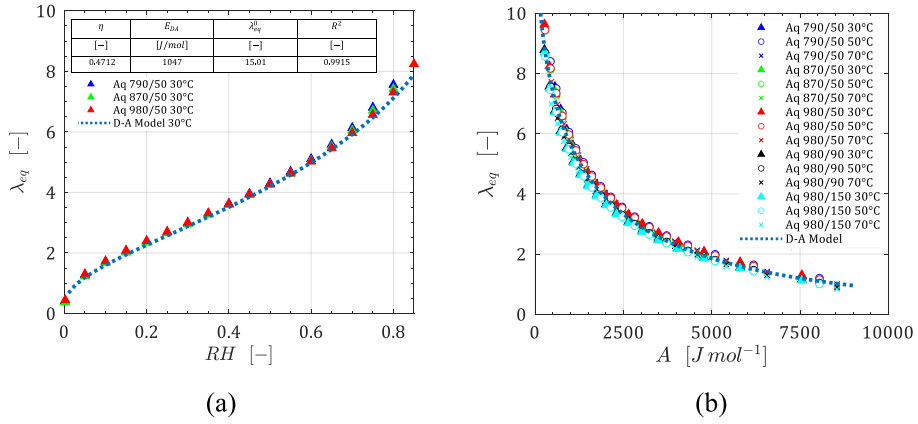

Fig. 2. (a) Sorption isotherms for different membranes, including parameters of DA model that best fits experimental sorption isotherms, also reported in Table 3; (b) Sorption isotherms as function of adsorption potential, A, and fitting with DA equations.

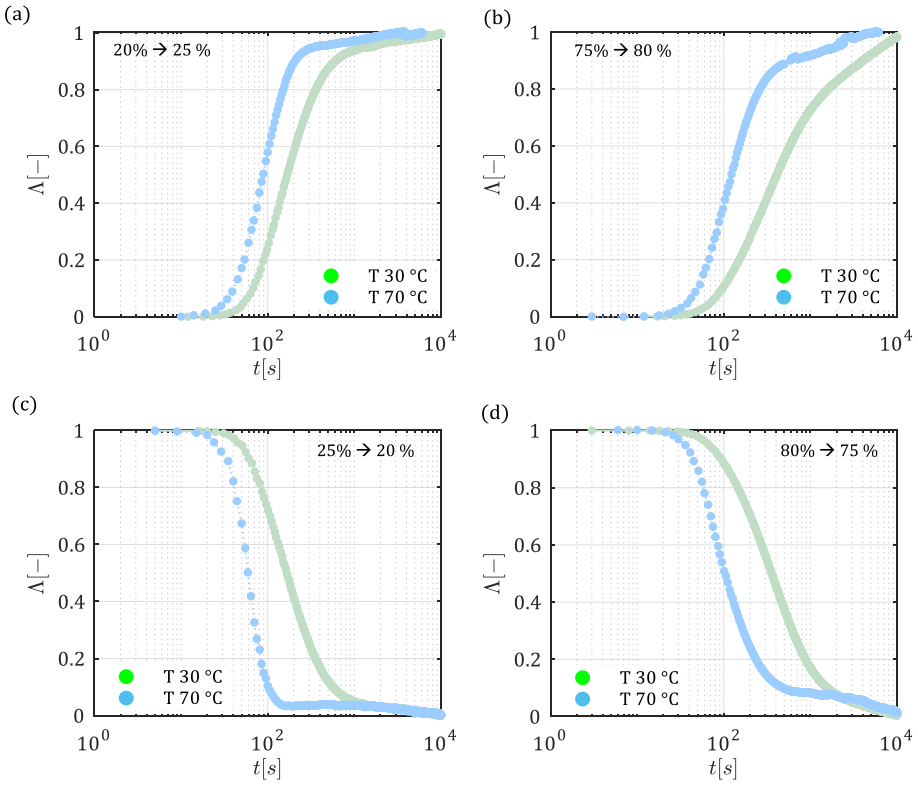

Fig. 3. DVS curves for Aquivion 980/50 during adsorption and desorption at different humidity intervals showing the normalized water content, Λ, change with time for 30 °C (green) and 70 °C (blue): (a) adsorption step from *RH* 20%–25%; (b) adsorption step from *RH* 75%–80%; (c) desorption step from *RH* 25%–20%; (d) desorption step from *RH* 80%–75%. (For interpretation of the references to colour in this figure legend, the reader is referred to the Web version of this article.)

Table 2
Numerical values obtained from fitting of Eq. (21) on experimental data, shown in Fig. 3.

Sorption phase	Adsorption				Desorption			
T [°C]	30°C		70°C		30°C		70°C	
RH step [%]	20→25	75→80	20→25	75→80	25→20	80→75	25→20	80→75
B [−]	0.055	0.248	0.074	0.220	0.045	0.089	0.034	0.091
τ_1 [s]	214	430	91	126	213	462	63	131
τ_2 [s]	4558	4500	1250	1200	4732	4730	1250	1550

reported in Section SI-3 of SI. At longer times, a second slow phenomenon controls water uptake: it can be attributed to the change in morphology of membrane, as consequence of the polymer rearrangement and relaxation [53]. Indeed, as time passes after a step in *RH*, polymer swelling/shrinking mechanism becomes the limiting rate step.

The semi-empirical method [53] shown in Eq. (21) is used to preliminary fit the two-stage sorption (adsorption and desorption) process: the terms τ_1 and τ_2, time constants related respectively to interfacial phenomena and polymer swelling, and the parameter B, related to the polymer swelling due to water uptake, are derived. Numerical values resulting from the regression of DVS curves of Fig. 3 are summarized in Table 2.

$$\Lambda = \begin{cases} 1-(1-B)\exp\left(-\dfrac{t}{\tau_1}\right) - B\exp\left(-\dfrac{t}{\tau_2}\right) & adsorption \\ (1-B)\exp\left(-\dfrac{t}{\tau_1}\right) + B\exp\left(-\dfrac{t}{\tau_2}\right) & desorption \end{cases} \quad (21)$$

Focusing on the polymer rearrangement process, the parameter B is highly sensitive to *RH*, suggesting that polymer swelling is more intense as *RH* increases, and no difference is appreciable as temperature changes. The time constant, τ_1, decreases as temperature increases, indicating that interfacial phenomena is a thermally activated process [24]. The same holds true for τ_2, governed by polymer relaxation [54]. Values of parameter B are slightly lower in desorption than during adsorption phase, mainly in the high *RH* regime. Tendency of polymer to adsorb water during the swelling is counterbalanced by the mechanical deformation of the matrix, which generates a swelling pressure. The adsorption process is hindered by the need for the structure to reorganize, whereas, the desorption process is promoted by swelling pressure and also favoured by the internal morphology and the connectivity of water domains at higher water contents [27]. On the contrary, τ_1 seems to be independent of the type of process (adsorption or desorption). The experimental evidence of a constitutive relation between material properties and operating conditions, discussed in this section, was used for deriving model parameters dependence in 3.2.3.

Table 3
Parameters for VVP and DVS models.

Model Parameters			
VVP model			
	Description	Value	Source
ξ_{mb}	Correction factor for $D_{v,m}$	$6.47 \times 10^{-6}\ m^2\ s^{-1}$	Calibrated
λ_{tp}	Turning point in $D_{v,m}$	2.15	Calibrated
δ_{tp}	Width of turning point	0.8758	[22]
ξ_{ad}	Correction factor for k_g	$0.66 \times 10^{-6}\ m\ s^{-1}$	[57]
E^k_{act}	Activation energy for k_g	$6\ kJ\ mol^{-1}$	Calibrated
d_{GDL}	Compressed GDL thickness	$1.75 \times 10^{-4}\ m$	Measured
E_{DA}	Characteristic energy in DA model	$1.047\ kJ\ mol^{-1}$	Calibrated
E^m_{act}	Activation energy for $D_{v,m}$	$27.8\ kJ\ mol^{-1}$	[22]
ε	GDL Porosity	0.75	Measured
ε_{pc}	Percolation threshold	0.11	[45]
h_{CH}	Channel height	$0.001\ m$	Measured
λ^0_{eq}	Reference water content in DA model	15.01	Calibrated
L_{CH}	Channel length	$0.15\ m$	Measured
n_e	Empirical constant for GDL effective diffusion	0.785	[45]
n_m	Characteristic parameter for $D_{v,m}$	− 2	[22]
η	Characteristic parameter in DA model	0.4712	Calibrated
ρ_m	Ionomer density	$1980\ kg\ m^{-3}$	[4]
w_{CH}	Channel width	$8.5 \times 10^{-4}\ m$	Measured
DVS model			
ξ_φ	Constant for φ	0.014	Calibrated
ξ_τ	Constant for τ_{relax}	0.067	Calibrated
E^s_{act}	Activation energy for τ_{relax}	$28.0\ kJ\ mol^{-1}$	Calibrated
h^{DVS}_m	Convective mass transfer coefficient in DVS	$2 \times 10^{-3}\ m\ s^{-1}$	Measured

3.2.2. Vapour-to-vapour permeation test

Results of vapour permeation tests of two Aquivion membranes (980/50 and 980/150) assembled with GDL H23I2 are analysed. Measurements are performed at two temperatures, 50 °C and 80 °C, denoted as Test VVP 50 and VVP 80. In Fig. 4(a), total water transport resistance, $R_{tot,v}$, is shown against membrane thickness, for different values of average relative humidity, RH^{avg}, for the two reference membranes with thickness equal to 50 μm and 150 μm. An average relative humidity, RH^{avg}, was estimated as shown in Eq. (22): given isothermal conditions on both sides, the average relative humidity on dry and wet side, RH^d and RH^w, was calculated with log-mean average between respective inlet and outlet *RH* [55]. RH^{avg} is used to get a semi-quantitative estimation of the membrane hydration, based on experimental data of different membranes.

$$RH^{avg} = \frac{RH^d + RH^w}{2} \quad (22)$$

Quite obviously, according to Fick's law, the higher the thickness, the higher the mass transfer resistance. To better evaluate the correlation between water transport resistance and membrane thickness, experimental results of the membrane assembly obtained with Aquivion 980/90 and the same porous media (GDL H23I2) are also shown (empty circles in Fig. 4(a)). These data are part of the results obtained for the additional membranes, discussed in section 3.3, but are anticipated in order to better understand the analysed physical phenomena. A linear dependence between $R_{tot,v}$ and membrane thickness can be appreciated in all the reported conditions. As RH^{avg} increases, the value of $R_{tot,v}$ decreases because of the effect of membrane hydration, which leads to an increase of its diffusivity and a decrease of M|GDL interface resistance, consistently with literature [56]. Accordingly, the higher RH^{avg}, the lower the slope of $R_{tot,v}$ versus d_m, as it is shown in the fitting lines of Fig. 4(a). In fact, the slope of such lines is inversely proportional to the average Fickian membrane diffusivity, $D_{v,m}$, indicating that it is highly dependent upon the average hydration in membrane. Finally, the analysis of the experimental results makes it possible to identify the main contributions of mass transport resistance, i.e. the diffusive and the interfacial one. Membrane thickness directly affects only the membrane diffusive resistance: as shown in Fig. 4(a), the intercept of the graph at d_m equal to zero represents the interfacial resistance, being the diffusive one null. The interfacial term is also inversely proportional to the average hydration of membrane [22,27].

In Fig. 4(b), permeated water flux, $\dot{m}_v$, is plotted against $\Delta C_{ml,v}$ for the two membrane assemblies and temperatures. The higher $\Delta C_{ml,v}$, the higher the permeated flux: the increase occurs more than linearly, suggesting that ionomer-related mass transport resistances are dependent upon its hydration state. The decrease in membrane thickness by three times allows to have a twofold value of permeated flux for the highest value of $\Delta C_{ml,v}$, because of the presence of additional contribution to total water-transport resistance that are not dependent on membrane thickness. Comparison between Tests VVP 50 and VVP 80 shows that for a given value of $\Delta C_{ml,v}$, the lower the temperature, the higher the permeated flux. This trend highlights that mass transport resistance decreases with membrane water content. In fact, comparing results obtained for each membrane assembly at a given $\Delta C_{ml,v}$, (for instance refer to values around 3.5 mol m^{-3} in Fig. 4(b)), the average *RH* on wet side is actually higher in the low temperature case, promoting membrane water uptake and, therefore, mass transport capacity, as in Ref. [23].

3.2.3. Model calibration

Calibration procedure is articulated in two phases, as shown in Fig. 5.

Initially, exploiting experimental data obtained on Aquivion 980/50 and 980/150, it has been possible to tune coefficients of Eqs. (6)–(8) to

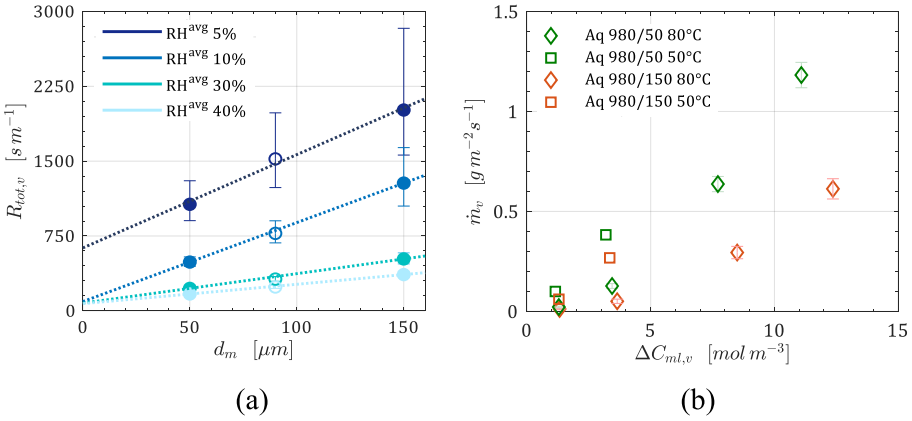

Fig. 4. (a) Resistance to steady-state water transport in the membrane as a function of membrane thickness for different average *RH*. Dashed lines are linear fittings. (b) VVP flux with respect to $\Delta C_{ml,v}$ for Aquivion 980/150 (red) and Aquivion 980/50 (green) at 50 °C and 80 °C, shown, respectively, with square symbols and diamond symbols. (For interpretation of the references to colour in this figure legend, the reader is referred to the Web version of this article.)

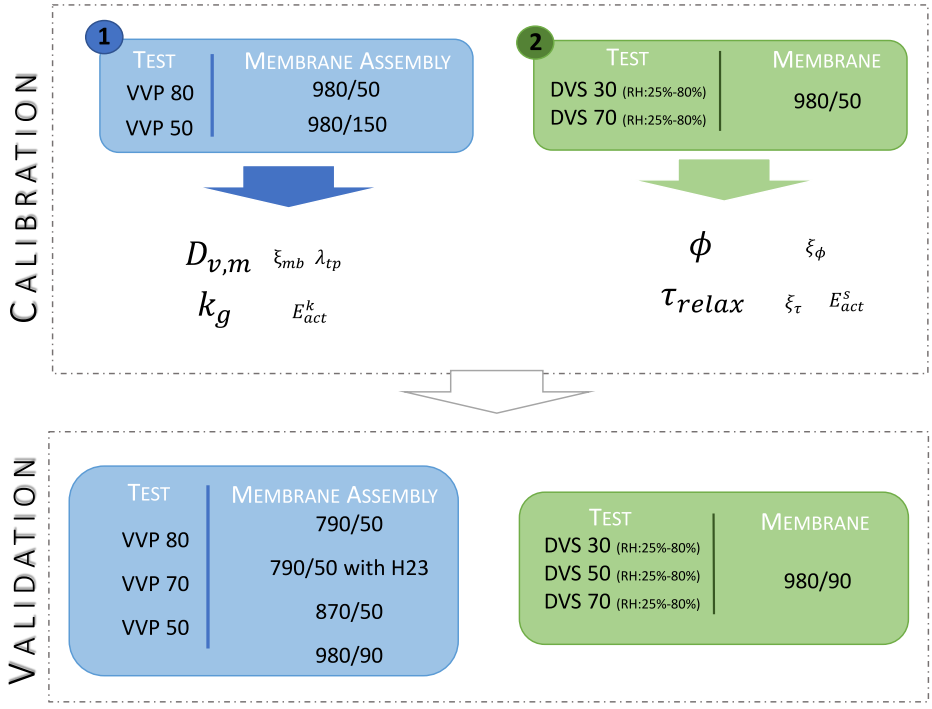

Fig. 5. Model calibration and validation procedure.

determine the dependence of $D_{v,m}$ and k_g upon the local hydration of ionomer. Objective function was the minimization of the error between experimental and numerical permeated flux for the given $\Delta C_{ml,v}$. Calibrated coefficients are reported in Table 3, together with all the other model parameters. The calibrated coefficients for $D_{v,m}$ are slightly higher with respect to the ones reported in literature, obtained from Nafion® [41]. The difference in material chemistries, since membranes in this study are belonging to SSC materials, justifies the slight increase in parameter values. The interfacial constant, k_g, resulting from the tuning procedure, is based on [57], where experimental data are obtained from state-of-the-art Nafion membranes. An Arrhenius-type dependence from temperature was added, as in Eq. (10), since data are collected at ambient temperature [57], and the activation energy, E^k_{act}, was tuned. Comparison between model simulations and experimental results for both Aquivion 980/50 and 980/150, indicates an optimal accordance, as visible in Fig. 6(c)–(d). Channel geometric dimensions are measured from experimental setup and GDL porosity is estimated on dedicated measurements, reported in Fig. 8, and it is in accordance with [58].

In the second step, swelling model parameters, φ and τ_{relax}, were investigated. As evidenced in Section 3.2.1, parameters B and τ_2 describe through a semi-empirical correlation, the effect of polymer swelling on water sorption/desorption and they are strictly correlated to model parameters, φ and τ_{relax}, quantifying similar information. Thus, the experimental outcomes about B and τ_2, describing their dependence on relative humidity, *RH*, and temperature, T, can be extended to φ and τ_{relax}, to develop proper semi-empirical correlations based on model variables, i.e. water content, λ, and temperature, T. As *RH* increases, the fraction of water that is furtherly absorbed/desorbed as result of polymer swelling/shrinking becomes more significant and a linear dependence from the water content is assumed. The final correlations for the two parameters are reported in Eq. (23) and Eq. (24).

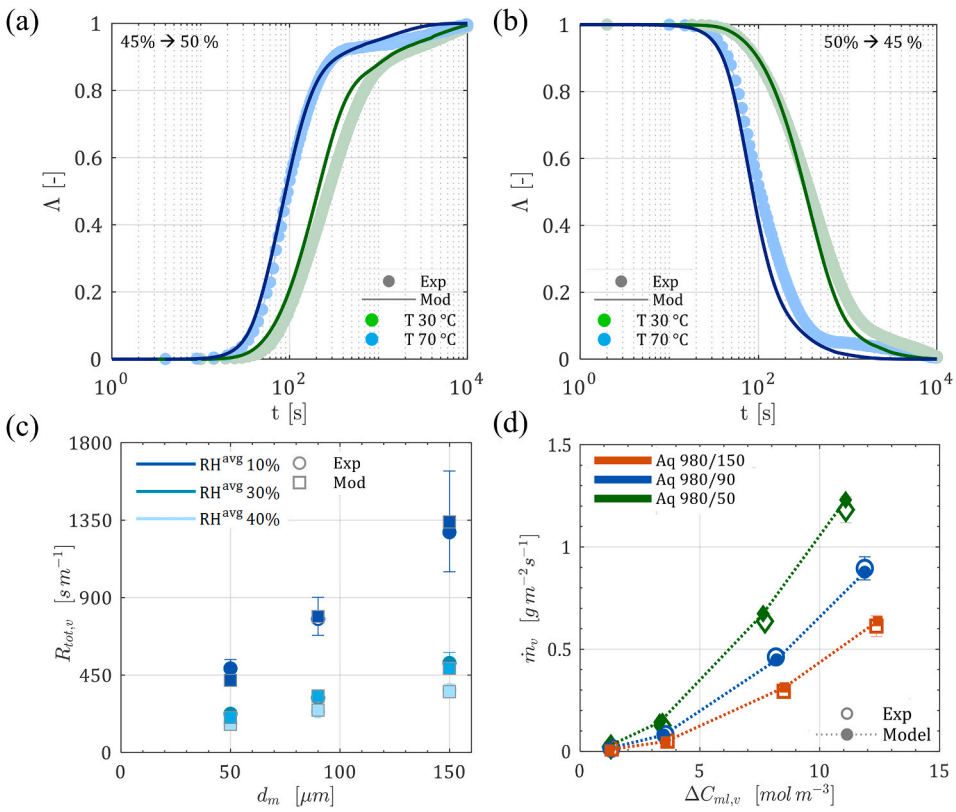

Fig. 6. (a–b) DVS curves for Aquivion 980/90 showing the normalized water content, Λ, change with time for 30 °C (green) and 70 °C (blue): (a) adsorption step from *RH* 45%–50%; (b) desorption step from *RH* 50%–45%. Comparison between model simulations, with solid lines, and experimental data, with dot symbols. (c) Experimental (circles) and simulated (squares) resistance to steady-state water transport in the membrane as a function of membrane thickness for different RH^{avg}; (d) Experimental and simulated VVP flux with respect to $\Delta C_{ml,v}$ for three different membrane thickness for VVP 80; experimental data with open symbols, model simulation with solid symbols and dashed line. (For interpretation of the references to colour in this figure legend, the reader is referred to the Web version of this article.)

$$\varphi = \xi_{\varphi}\lambda \tag{23}$$

Model parameter φ is strictly linked to the swelling mechanism. Focusing on τ_{relax}, an Arrhenius-type equation was adopted, describing the decrease in time constant as temperature increases. Moreover, τ_{relax} is assumed to be lower during desorption with respect to adsorption; specifically relaxation time τ_{relax} is halved during desorption phase with respect to adsorption, consistently with [30], where adsorption process is found to be twice as slower as the desorption one.

$$\tau_{relax} = \begin{cases} \xi_{\tau} \exp\left(\dfrac{E^{s}_{act}}{\mathscr{R}T}\right) & adsorption \\ \dfrac{\xi_{\tau}}{2} \exp\left(\dfrac{E^{s}_{act}}{\mathscr{R}T}\right) & desorption \end{cases} \tag{24}$$

Tuning of parameters ξ_{φ}, ξ_{τ} and E^{s}_{act} was, thus, performed by minimizing the error between experimental and numerical values of normalized water content, Λ, evaluated in the cases shown in Fig. 3. Comparison between model simulations and experimental results, both for sorption and desorption curves, indicates an optimal accordance and it is reported in SI. Then, for the DVS setup, an average value of 2×10^{-3} m s^{-1} was found for h_m^{DVS}, consistent with data found in the literature for similar apparatus [59].

3.3. Additional membranes: model validation and detailed investigation

3.3.1. Membrane thickness

In Fig. 6(a and b), transient adsorption and desorption of normalized water content Λ for Aquivion 980/90 is shown. Experimental data and numerical results are evaluated for selected *RH* step at 30 °C and 70 °C, different from ones adopted in the calibration process. Results confirm the reliability of the expressions obtained for φ and τ_{relax}, (Eq. (23) and Eq. (24)), demonstrating a consistent physical description of swelling phenomena with experimental data for the different humidity ranges and temperatures. In Fig. 6(c) the calculated and measured mass transfer resistance, $R_{tot,v}$, is reported for different values of RH^{avg}. In Fig. 6(d), the comparison between simulated and experimental steady state water flux, as a function of the logarithmic mean vapour concentration, is reported for the three membranes 980/50, 980/90 and 980/150. Results are consistent with experimental data. Different contributions to the total resistance have been computed through model simulations, according to the method presented in Ref. [60] and reported in SI. Membrane diffusion resistance is almost threefold for the thicker sample (150 μm) than to the thinner one (50 μm), since $D_{v,m}$ is similar because related to RH^{avg}. Instead, the interfacial resistance, mainly at the dry side, is higher for the thicker membrane. In fact, even if the average water content is almost equal due to the same RH^{avg}, a different distribution occurs along membrane thickness: low values of λ are present on the dry side in case of thick membrane, determining a higher interfacial mass transport resistance. A similar inverted trend is shown on wet side: in this case, due to high local values of λ, interfacial resistance is low in both membranes.

Finally, it is noted that the contribution of interfacial resistances respect $R_{v,tot}$ is around 20% and 17% respectively for Aquivion 980/50 and 980/150, confirming the increased contribution of interfacial resistance as membrane thickness decreases. It is worth specifying that channel convective and the GDLs diffusive resistances are not affected by membrane thickness.

3.3.2. Equivalent weight

The analysis of *EW* was performed exploiting data from Test VVP 80, obtained on Aquivion 980/50, 870/50, 790/50. Fig. 7(a) highlights the effect of *EW* on water transport through the ionomer: the lower *EW*, the lower the total water transport resistance, in particular at low RH^{avg}. Calculated $R_{tot,v}$ values from model simulation are consistent with ones determined from experimental data, with maximum relative difference of 11% shown in the case of RH^{avg} equal to 10%. It should be noted that the numerical results always fall within the uncertainty band of the experimental data. In Fig. 7(b), comparison between simulated and

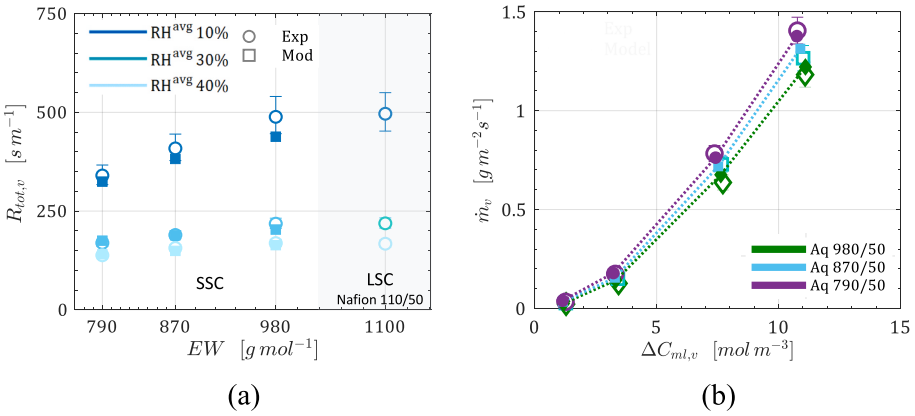

Fig. 7. (a) Experimental (void circles) and simulated (full squares) resistance to steady-state water transport in the membrane as a function of membrane *EW* for different average *RH*; (b) Experimental and simulated VVP flux with respect to $\Delta C_{ml,v}$ for Test VVP 80; experimental data with open symbols, model simulation with solid symbols and dashed line.

experimental permeated flux is reported for the three membranes: good agreement is shown with relative difference within 5%. Therefore, it can be concluded that the model adequately reproduces the effect of *EW* on water transport phenomena.

A detailed investigation of local water transport contributions highlights that, at given operating conditions, the lower *EW*, the lower both membrane diffusive and interfacial resistances. In particular, if *EW* is reduced from 980 g mol^{-1} to 790 g mol^{-1}, the diffusive resistance decreases of 18% and the interfacial resistances decrease of 11% and 46%, respectively on wet and dry side. In fact, at constant λ, the lower *EW*, the higher the concentration of sulfonic acid groups, and, consequently, the higher the average water concentration inside the membrane (according to Eq. (5)). It is reported in literature that *EW* affects nanomorphology of PFSA ionomer: an increase in *EW* leads to a more homogeneous packing of hydrophobic and hydrophilic domains [61]. A study about molecular dynamic simulations discussing microphase separation within hydrated Nafion membranes [62] highlights that mobility of water molecules inside the hydrophilic pores is higher when *EW* is reduced. Moreover, in case of low *EW*, a greater dispersion of the water clusters is visible inside the ionomer matrix when water hydration increases [63]. The Fickian diffusion coefficient, $D_{v,m}$, increases with water mobility through the hydrophilic clusters and decreases with dispersion of clusters. As a final result, in case of low *EW*, $D_{v,m}$ decreases slightly, according to Eq. (6) and confirming the relevance of morphological features and changes. On the other side, since the water activity is assumed as the driving force of water transport, the membrane diffusive resistance is proportional to the term $EW/(D_{v,m}\,\rho_m)$, as also visible in SI. The decrease in *EW* exceeds the reduction of $D_{v,m}$, leading to the aforementioned reduction of diffusive resistance. The low *EW* is also beneficial for interfacial resistance, leading to an increase of k_g due to previously discussed improvement of water mobility. A higher water content occurs on both dry and wet sides, favouring the overall membrane hydration.

Finally, total mass transport resistance of Nafion 1100/50 is reported in Fig. 7(a), besides the three investigated membranes. Actually, water permeation resistance of Nafion 1100/50 is similar to one of Aquivion 980/50. This trend can be explained evaluating morphology of hydrophilic water channels. The specific pore area of water channels was found to decrease with *EW* [62,64]. At the same time, water channels of Nafion ionomer own a more straight morphology and less necking points compared to ones of Aquivion polymer [61]. Those two features could compensate each other, determining a comparable water permeated flux.

Since the effect of *EW* on dynamic adsorption was found to be limited, this aspect is not discussed in detail in this section. More information is however available in SI.

3.3.3. Porous layer treatment

The effect of porous layer on water transport was investigated, selecting as reference membrane the Aquivion 790/50, which exhibited the lowest water transfer resistance among those tested. Two membrane assemblies, with different GDLs, were analysed. The adopted GDLs, namely H23 and H23I2, differ mainly for the surface treatment, which leaves the former slightly hydrophilic and makes the latter hydrophobic [33]. In Fig. 8(a), total water mass transport resistance for two values of average RH^{avg}, equal to 10% and 40%, is plotted against the thickness of GDLs. $R_{tot,v}$ linearly increases with the thickness for both GDLs and, in addition, slopes are not affected by RH^{avg}. The effective water diffusivity through the GDLs, evaluated at the reference temperature of 70 °C and in accordance with literature [65], was estimated to be around 1.8×10^{-5} m^2 s^{-1} and 2.1×10^{-5} m^2 s^{-1}, respectively for hydrophobic and hydrophilic superficial treatment. The intercepts in Fig. 8(a) represent all the resistances except for GDLs diffusive ones. Such values are highly sensitive to average RH^{avg} and GDLs characteristics, ranging from 90 to 340 s m^{-1} in the investigated conditions. Since effect on GDL diffusive resistance is negligible, because of similar water diffusivity, it was, thus, inferred that GDL treatment acts on the water transport at the membrane-GDL interface. At microscopic level, there is evidence in literature that ionomer surface water transport behaves similarly to a hydrophilic interface when local water content increases [66], suggesting that the interfacial resistance is controlled by the accessibility of the hydrophilic surface domains. The presence of a hydrophilic environment close to membrane surface, such as in case of hydrophilic GDL, promotes the access to transport channels inside the ionomer. Therefore, although water vapour diffusivity across the two GDLs is almost equal, the use of a hydrophilic component has significant effects on the reduction of the interfacial resistance. To support this hypothesis, it is put in evidence that when hydrophobic GDLs are substituted with hydrophilic ones, a reduction in $R_{tot,v}$ around 22% is shown. This decrease is comparable with the contribution given by interfacial resistances on the same $R_{tot,v}$, found to be equal to 20%, as discussed in Section 3.3.1.

In Fig. 8(b), it is shown the permeated water flux for the two different configurations. According to previous analysis, membrane assembly with hydrophilic GDLs has proved to have the best performance for all temperature and *RH* conditions, reaching a water flux up to 30% higher than one of hydrophobic GDLs. Experimental results obtained with the hydrophilic GDLs have been consistently reproduced by the proposed model, resulting in a negligible interfacial resistance.

Moreover, very low interfacial resistance has been observed when membrane is in contact with liquid water [67]. The developed

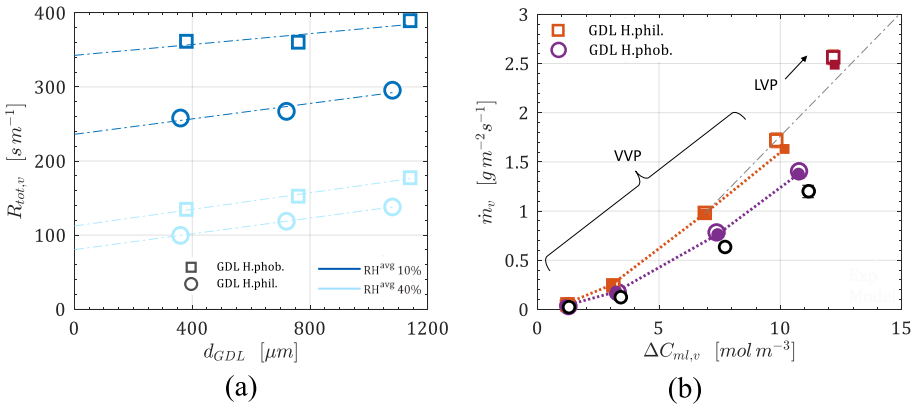

Fig. 8. (a) Resistance to steady-state water transport on Aquivion 790/50 as a function of GDL thickness for different average *RH* and fitting lines (b) Experimental and simulated VVP flux with respect to $\Delta C_{ml,v}$ for Test VVP 80 and LVP 80 on Aquivion 790/50 in combination with hydrophilic (GDL H.phil) and hydrophobic (GDL H.phob) GDLs; experimental VVP flux with respect to $\Delta C_{ml,v}$ for Test VVP 80 for Nafion 212, assembled together with hydrophobic GDL, is reported for comparison with benchmark with black open symbols; experimental data with open symbols, model simulation with solid symbols and dashed line.

phenomenological model has been used to simulate water mass transport across membrane assuming negligible interfacial resistance and infinite wet airflow (vapour concentration, C_v^w, is assumed to be in saturated conditions both at inlet and outlet). Result has been compared with one of an additional experimental test to evaluate liquid to vapour permeation (LVP). Such test was conducted on the same membrane assembly, consisting of Aquivion 790/50 together with hydrophilic GDLs, with liquid water on the wet side and dry air on the other side. The additional LVP data are reported in Fig. 8(b): numerical and experimental values are very close (difference within 4%), confirming that interfacial resistance is negligible in case of liquid permeation and comparable with one obtained in case of vapour permeation and hydrophilic GDLs.

4. Conclusions

Water transport in PFSA Aquivion membranes was deeply investigated through a proper integration of experimental data and results of a phenomenological model. Analysis has been carried out both in steady state and dynamic conditions. The 1D+1D model of membrane assembly, based on one available in literature for Nafion, has been properly modified and implemented to simulate both the VVP and DVS experiments with Aquivion based membranes. The model was calibrated with experimental data of a reference membrane and validated with further data of additional membranes. In particular, VVP data have been used to calibrate three parameters related to diffusion and interfacial transport and DVS data to determine adsorption isotherm correlations and to fit three parameters related to swelling process due to membrane hydration. Then, model validation was achieved by simulating both steady-state permeation and DVS tests. With the aid of the validated model, each contribution to water mass transfer has been investigated and quantified. Main findings of the research are hereinafter reported:

- Steady state and dynamic water transport in membranes has been deeply investigated and related to material and constitutive properties of membranes.
- Contribution of swelling process to dynamic water transport increases with membrane hydration and its characteristic time decreases with increasing temperature.
- The lower the membrane thickness, the higher the water mass transport. In particular, total mass transfer resistance reduces by 47% when thickness of Aquivion 980 membranes passes from 150 μm to 50 μm, due to non-negligible interfacial resistances.
- A membrane with low *EW* presents a higher water-transfer capacity. In the investigated cases, *EW* impacts on diffusive and, particularly, on interfacial resistances, which reduce respectively by 18% and 30% when membrane *EW* passes from 980 g mol^{-1} to 790 g mol^{-1}.
- In case of hydrophobic GDLs, interfacial water transfer resistances contribute to around 20% of the total. Instead, in case of hydrophilic GDLs the interfacial resistance was found to be negligible.
- New correlations for the dynamic water transport model of Aquivion membranes, including polymer swelling, are proposed. Such correlations can be easily implemented in models of typical electrochemical devices, such as PEMFCs and PEMWEs, particularly for membrane and catalyst layers. It should be noted that for the latter, additional studies are necessary to highlight differences when dealing with thin films in the catalyst layer.

CRediT authorship contribution statement

Amedeo Grimaldi: Conceptualization, Methodology, Software, Validation, Investigation, Data curation, Visualization, Writing – original draft, Writing – review & editing. **Andrea Baricci:** Investigation, Methodology, Writing – review & editing. **Stefano De Antonellis:** Investigation, Methodology, Writing – original draft, Writing – review & editing. **Claudio Oldani:** Resources, Methodology, Writing – review & editing. **Andrea Casalegno:** Conceptualization, Methodology, Writing – review & editing.

Declaration of competing interest

The authors declare the following financial interests/personal relationships which may be considered as potential competing interests: Claudio Oldani reports a relationship with Solvay Specialty Polymers SpA that includes: employment.

Data availability

Data will be made available on request.

Acknowledgements

The research leading to these results has received funding from the Energy for Motion initiative of Politecnico di Milano as part of Energy department recognition as Department of Excellence 2018–2020 from Italian Ministry of Education, Universities and Research (MIUR).

Appendix A. Supplementary data

Supplementary data to this article can be found online at https://doi.org/10.1016/j.jpowsour.2022.232556.

Nomenclature

A	Adsorption potential in Dubinin-Astakhov model / J mol^{-1}
B	Characteristic parameter for two-stage sorption equation
C	Gas concentration / mol m^{-3}
d	Thickness / m
d_h	Hydraulic diameter of gas channel / m
$D_{i,k}$	Fickian water diffusion coefficient of species i in layer k / m^2 s^{-1}
D_{ij}	Binary diffusion coefficient of gas species i in j / m^2 s^{-1}
E_{act}	Activation energy / J mol^{-1}
E_{DA}	Characteristic energy of adsorption in Dubinin-Astakhov model / J mol^{-1}
EW	Equivalent weight of ionomer / g mol^{-1}
f	Friction factor for pressure losses
h_{CH}	Channel height / m
k_g	Interfacial constant of water sorption / m s^{-1}
L_{CH}	Channel length / m
m	Mass / g
$\dot{m}$	Mass flux per unit area of membrane / g m^{-2} s^{-1}
$\dot{M}$	Mass flux / g s^{-1}
MM	Molecular weight / g mol^{-1}
n	Number of moles / mol
n_e	Empirical constant for GDL effective diffusion coefficient
n_m	Characteristic parameter for $D_{v,m}$
p	Gas pressure / Pa
p_{vsat}	Saturation pressure / Pa
$R_{i,v}$	VVP steady-state resistance of layer i / s m^{-1}
$\mathcal{R}$	Universal gas constant / J mol^{-1} K^{-1}
RH	Relative humidity of gas
s_{relax}	Characteristic variable of swelling model
T	Temperature / K
V	Volume / m^3
$\dot{V}$	Volumetric flow rate / NL min^{-1}
$\overline{V}$	Molar volume / m^3 mol^{-1}
y	Molar fraction

Greek letters

ϵ_{pc}	Percolation threshold for GDL diffusion coefficient
Δ	Difference
ε	GDL porosity
η	Characteristic parameter in Dubinin-Astakhov model
λ	Water content in membrane
μ	Gas dynamic viscosity / Pa s
ρ	Density / g m^{-3}
τ	Time constant / s
φ	Swelling coefficient

Superscripts

avg	Average
d	Dry
in	Inlet
out	Outlet
w	Wet

Subscripts

H_2O	Water
a	Anhydrous
ads	Adsorption phase
air	Dry air
des	Desorption phase
dp	Dew point
eq	Equilibrium conditions

l	Liquid water
m	Membrane
ml	Mean logarithmic
tot	Total
v	Water vapour

Acronyms

CL	Catalyst layer
DA	Dubinin-Astakhov model
DVS	Dynamic vapour sorption
GDL	Gas diffusion layer
LVP	Liquid-to-vapour permeation
M	Membrane
PEMFC	Proton-exchange membrane fuel cell
PEMWE	Proton-exchange membrane water electrolyser
PFSA	Perfluorosulfonic acid
SSC	Short-side-chain
VVP	Vapour-to-vapour permeation

References

[1] C.J. Lee, J. Song, K.S. Yoon, Y. Rho, D.M. Yu, K.H. Oh, J.Y. Lee, T.H. Kim, Y. T. Hong, H.J. Kim, S.J. Yoon, S. So, Controlling hydrophilic channel alignment of perfluorinated sulfonic acid membranes via biaxial drawing for high performance and durable polymer electrolyte membrane water electrolysis, J. Power Sources 518 (2022), 230772, https://doi.org/10.1016/j.jpowsour.2021.230772.

[2] A. Ly, T. Asset, P. Atanassov, Integrating nanostructured Pt-based electrocatalysts in proton exchange membrane fuel cells, J. Power Sources 478 (2020), 228516, https://doi.org/10.1016/j.jpowsour.2020.228516.

[3] A. Baricci, A. Bisello, A. Serov, M. Odgaard, P. Atanassov, A. Casalegno, Analysis of the effect of catalyst layer thickness on the performance and durability of platinum group metal-free catalysts for polymer electrolyte membrane fuel cells, Sustain. Energy Fuels 3 (2019) 3375–3386, https://doi.org/10.1039/C9SE00252A.

[4] A. Kusoglu, A.Z. Weber, New insights into perfluorinated sulfonic-acid ionomers, Chem. Rev. 117 (2017) 987–1104, https://doi.org/10.1021/acs.chemrev.6b00159.

[5] P. Gazdzick, J. Mitzel, D. Garcia Sanchez, M. Schulze, K.A. Friedrich, Evaluation of reversible and irreversible degradation rates of polymer electrolyte membrane fuel cells tested in automotive conditions, J. Power Sources 327 (2016) 86–95, https://doi.org/10.1016/j.jpowsour.2016.07.049.

[6] D.A. Cullen, K.C. Neyerlin, R.K. Ahluwalia, R. Mukundan, K.L. More, R.L. Borup, A. Z. Weber, D.J. Myers, A. Kusoglu, New roads and challenges for fuel cells in heavy-duty transportation, Nat. Energy 6 (2021) 462–474, https://doi.org/10.1038/s41560-021-00775-z.

[7] S. Touhami, M. Crouillere, J. Mainka, J. Dillet, C. Nayoze-Coynel, C. Bas, L. Dubau, A. El Kaddouri, F. Dubelley, F. Micoud, M. Chatenet, Y. Bultel, O. Lottin, Anode defects' propagation in polymer electrolyte membrane fuel cells, J. Power Sources 520 (2022), 230880, https://doi.org/10.1016/j.jpowsour.2021.230880.

[8] J. Xie, D.L. Wood, D.M. Wayne, T.A. Zawodzinski, P. Atanassov, R.L. Borup, Durability of PEFCs at high humidity conditions, J. Electrochem. Soc. 152 (2005) A104, https://doi.org/10.1149/1.1830355.

[9] J. Xie, D.L. Wood, K.L. More, P. Atanassov, R.L. Borup, Microstructural changes of membrane electrode assemblies during PEFC durability testing at high humidity conditions, J. Electrochem. Soc. 152 (2005) A1011, https://doi.org/10.1149/1.1873492.

[10] J.P. Braaten, N.N. Kariuki, D.J. Myers, S. Blackburn, G. Brown, A. Park, S. Litster, Integration of a high oxygen permeability ionomer into polymer electrolyte membrane fuel cell cathodes for high efficiency and power density, J. Power Sources 522 (2022), 230821, https://doi.org/10.1016/j.jpowsour.2021.230821.

[11] S. Ma, Y. Qin, Y. Liu, L. Sun, Q. Guo, Y. Yin, Delamination evolution of PEM fuel cell membrane/CL interface under asymmetric RH cycling and CL crack location, Appl. Energy 310 (2022), 118551, https://doi.org/10.1016/j.apenergy.2022.118551.

[12] N.S. Khattra, S. Bhattacharya, M.V. Lauritzen, E. Kjeang, Residual fatigue life modeling of fuel cell membranes, J. Power Sources 477 (2020), 228714, https://doi.org/10.1016/j.jpowsour.2020.228714.

[13] W. Yoon, X. Huang, A nonlinear viscoelastic-viscoplastic constitutive model for ionomer membranes in polymer electrolyte membrane fuel cells, J. Power Sources 196 (2011) 3933–3941, https://doi.org/10.1016/j.jpowsour.2010.12.034.

[14] A. Sadeghi Alavijeh, S. Bhattacharya, O. Thomas, C. Chuy, Y. Yang, H. Zhang, E. Kjeang, Effect of hygral swelling and shrinkage on mechanical durability of fuel cell membranes, J. Power Sources 427 (2019) 207–214, https://doi.org/10.1016/j.jpowsour.2019.04.081.

[15] S. Siracusano, V. Baglio, E. Moukheiber, L. Merlo, A.S. Arico, Performance of a PEM water electrolyser combining an IrRu-oxide anode electrocatalyst and a shortside chain Aquivion membrane, Int. J. Hydrogen Energy 40 (2015) 14430–14435, https://doi.org/10.1016/j.ijhydene.2015.04.159.

[16] X. Luo, S. Holdcroft, Water transport through short side chain perfluorosulfonic acid ionomer membranes, J. Membr. Sci. 520 (2016) 155–165, https://doi.org/10.1016/j.memsci.2016.07.021.

[17] M.B. Satterfield, J.B. Benziger, Non-fickian water vapor sorption dynamics by nafion membranes, J. Phys. Chem. B 112 (2008) 3693–3704, https://doi.org/10.1021/jp7103243.

[18] P. Majsztrik, A. Bocarsly, J. Benziger, Water permeation through nafion membranes: the role of water activity, J. Phys. Chem. B 112 (2008) 16280–16289, https://doi.org/10.1021/jp804197x.

[19] S. Ge, X. Li, B. Yi, I.-M. Hsing, Absorption, desorption, and transport of water in polymer electrolyte membranes for fuel cells, J. Electrochem. Soc. 152 (2005) A1149, https://doi.org/10.1149/1.1899263.

[20] Q. Zhao, P. Majsztrik, J. Benziger, Diffusion and interfacial transport of water in Nafion, J. Phys. Chem. B 115 (2011) 2717–2727, https://doi.org/10.1021/jp1112125.

[21] N.S. Schneider, D. Rivin, Steady state analysis of water vapor transport in ionomers, Polymer 51 (2010) 671–678, https://doi.org/10.1016/j.polymer.2009.12.005.

[22] V. Liso, S. Simon Araya, A.C. Olesen, M.P. Nielsen, S.K. Kær, Modeling and experimental validation of water mass balance in a PEM fuel cell stack, Int. J. Hydrogen Energy 41 (2016) 3079–3092, https://doi.org/10.1016/j.ijhydene.2015.10.095.

[23] F. Wolfenstetter, M. Kreitmeir, L. Schoenfeld, H. Klein, M. Becker, S. Rehfeldt, Experimental study on water transport in membrane humidifiers for polymer electrolyte membrane fuel cells, Int. J. Hydrogen Energy (2022), https://doi.org/10.1016/j.ijhydene.2022.05.114.

[24] R. Vetter, J.O. Schumacher, Experimental parameter uncertainty in proton exchange membrane fuel cell modeling. Part I: scatter in material parameterization, J. Power Sources 438 (2019), 227018, https://doi.org/10.1016/j.jpowsour.2019.227018.

[25] D.J. Burnett, A.R. Garcia, F. Thielmann, Measuring moisture sorption and diffusion kinetics on proton exchange membranes using a gravimetric vapor sorption apparatus, J. Power Sources 160 (2006) 426–430, https://doi.org/10.1016/j.jpowsour.2005.12.096.

[26] P.M. Mangiagli, C.S. Ewing, K. Xu, Q. Wang, M.A. Hickner, Dynamic water uptake of flexible ion-containing polymer networks, Fuel Cell. 9 (2009) 432–438, https://doi.org/10.1002/fuce.200800157.

[27] A. Kusoglu, A.Z. Weber, Water transport and sorption in nafion membrane, in: Polym. Energy Storage Deliv. Polyelectrolytes Batter. Fuel Cells, ACS Publications, 2012, pp. 175–199, https://doi.org/10.1021/bk-2012-1096.ch011.

[28] V. Klika, J. Kubant, M. Pavelka, J.B. Benziger, Non-equilibrium thermodynamic model of water sorption in Nafion membranes, J. Membr. Sci. 540 (2017) 35–49, https://doi.org/10.1016/j.memsci.2017.06.025.

[29] A. Goshtasbi, B.L. Pence, J. Chen, M.A. DeBolt, C. Wang, J.R. Waldecker, S. Hirano, T. Ersal, A mathematical model toward real-time monitoring of automotive PEM fuel cells, J. Electrochem. Soc. 167 (2020), 024518, https://doi.org/10.1149/1945-7111/ab6dd1.

[30] T.J. Silverman, J.P. Meyers, J.J. Beaman, Modeling water transport and swelling in polymer electrolyte membranes, ECS Trans. 28 (2010) 17–30, https://doi.org/10.1149/1.3490299.

[31] M. Fumagalli, S. Lyonnard, G. Prajapati, Q. Berrod, L. Porcar, A. Guillermo, G. Gebel, Fast water diffusion and long-term polymer reorganization during nafion membrane hydration evidenced by time-resolved small-angle neutron scattering, J. Phys. Chem. B 119 (2015) 7068–7076, https://doi.org/10.1021/acs.jpcb.5b01220.

[32] A. Rolfi, C. Oldani, L. Merlo, D. Facchi, R. Ruffo, New perfluorinated ionomer with improved oxygen permeability for application in cathode polymeric electrolyte membrane fuel cell, J. Power Sources 396 (2018) 95–101, https://doi.org/10.1016/j.jpowsour.2018.05.093.

[33] Freudenberg Performance Materials, Freudenberg gas diffusion layers GDL recommendation for LT-PEMFC applications. http://fuelcellsetc.com/store/DS/freudenberg.pdf, 2019. (Accessed 11 August 2022).
[34] T. Cahalan, S. Rehfeldt, M. Bauer, M. Becker, H. Klein, Experimental set-up for analysis of membranes used in external membrane humidification of PEM fuel cells, Int. J. Hydrogen Energy 41 (2016) 13666–13677, https://doi.org/10.1016/j.ijhydene.2016.05.281.
[35] S. Galbiati, A. Baricci, A. Casalegno, R. Marchesi, Experimental study of water transport in a polybenzimidazole-based high temperature PEMFC, Int. J. Hydrogen Energy 37 (2011) 2462–2469, https://doi.org/10.1016/j.ijhydene.2011.09.159.
[36] ISO/IEC, Uncertainty of Measurement Part 3 : Guide to the Expression of Uncertainty in Measurement (GUM:1995), 2008.
[37] A.C. Olesen, T. Berning, S.K. Kær, On the diffusion coefficient of water in polymer electrolyte membranes, ECS Trans. 50 (2013) 979–991, https://doi.org/10.1149/05002.0979ecst.
[38] M.A. Raso, T.J. Leo, O. González-Espasandín, E. Navarro, New expressions to determine the water diffusion coefficient in the membrane of PEM fuel cells, Int. J. Hydrogen Energy 41 (2016) 19766–19770, https://doi.org/10.1016/j.ijhydene.2016.05.075.
[39] T.E. Springer, T.A. Zawodzinski, S. Gottesfeld, Polymer electrolyte fuel cell model, J. Electrochem. Soc. 138 (1991) 2334–2342, https://doi.org/10.1149/1.2085971.
[40] A.A. Kulikovsky, Quasi-3D modeling of water transport in polymer electrolyte fuel cells, J. Electrochem. Soc. 150 (2003) A1432, https://doi.org/10.1149/1.1611489.
[41] A.C. Olesen. Macroscopic Modeling of Transport Phenomena in Direct Methanol Fuel Cells, Aalborg University, 2013. https://vbn.aau.dk/en/publications/macroscopic-modeling-of-transport-phenomena-in-direct-methanol-fu.
[42] A.A. Kalinnikov, S.A. Grigoriev, D.G. Bessarabov, Nonequilibrium poroelectroelastic theory for polymer electrolytes under conditions of water electrolysis, Int. J. Hydrogen Energy 44 (2019) 7889–7904, https://doi.org/10.1016/j.ijhydene.2019.02.025.
[43] A. Goshtasbi, Modeling, Parameter Identification, and Degradation-Conscious Control of Polymer Electrolyte Membrane (PEM) Fuel Cells, University of Michigan, 2019. https://hdl.handle.net/2027.42/155288.
[44] S.G. Chen, R.T. Yang, Theoretical basis for the potential theory adsorption isotherms. The dubinin-radushkevich and dubinin-astakhov equations, Langmuir 10 (1994) 4244–4249, https://doi.org/10.1021/la00023a054.
[45] N. Zamel, X. Li, J. Becker, A. Wiegmann, Effect of liquid water on transport properties of the gas diffusion layer of polymer electrolyte membrane fuel cells, Int. J. Hydrogen Energy 36 (2011) 5466–5478, https://doi.org/10.1016/j.ijhydene.2011.01.146.
[46] E.N. Fuller, P.D. Schettler, J.C. Giddings, A new method for prediction of binary gas-phase diffusion coefficients, Ind. Eng. Chem. 58 (1966) 18–27, https://doi.org/10.1021/ie50677a007.
[47] L.M. Pant, M.R. Gerhardt, N. Macauley, R. Mukundan, R.L. Borup, A.Z. Weber, Along-the-channel modeling and analysis of PEFCs at low stoichiometry: development of a 1+2D model, Electrochim. Acta 326 (2019), https://doi.org/10.1016/j.electacta.2019.134963.
[48] D.W. Green, M.Z. Southard (Eds.), Perry's Chemical Engineers' Handbook, ninth ed., McGraw-Hill Education, New York, 2019. https://www.accessengineeringlibrary.com/content/book/9780071834087.
[49] A. Kusoglu, T.J. Dursch, A.Z. Weber, Nanostructure/swelling relationships of bulk and thin-film PFSA ionomers, Adv. Funct. Mater. 26 (2016) 4961–4975, https://doi.org/10.1002/adfm.201600861.
[50] M.G. De Angelis, S. Lodge, M. Giacinti Baschetti, G.C. Sarti, F. Doghieri, A. Sanguineti, P. Fossati, Water sorption and diffusion in a short-side-chain perfluorosulfonic acid ionomer membrane for PEMFCS: effect of temperature and pre-treatment, Desalination 193 (2006) 398–404, https://doi.org/10.1016/j.desal.2005.06.070.
[51] N. Ramaswamy, S. Kumaraguru, R. Koestner, T. Fuller, W. Gu, N. Kariuki, D. Myers, P.J. Dudenas, A. Kusoglu, Editors' choice—ionomer side chain length and equivalent weight impact on high current density transport resistances in PEMFC cathodes, J. Electrochem. Soc. 168 (2021), 024518, https://doi.org/10.1149/1945-7111/abe5eb.
[52] X. Luo, G. Lau, M. Tesfaye, C.R. Arthurs, I. Cordova, C. Wang, M. Yandrasits, A. Kusoglu, Thickness dependence of proton-exchange-membrane properties, J. Electrochem. Soc. 168 (2021), 104517, https://doi.org/10.1149/1945-7111/ac2973.
[53] P.W. Majsztrik, M.B. Satterfield, A.B. Bocarsly, J.B. Benziger, Water sorption, desorption and transport in Nafion membranes, J. Membr. Sci. 301 (2007) 93–106, https://doi.org/10.1016/j.memsci.2007.06.022.
[54] Y. Zheng, U. Ash, R.P. Pandey, A.G. Ozioko, J. Ponce-González, M. Handl, T. Weissbach, J.R. Varcoe, S. Holdcroft, M.W. Liberatore, R. Hiesgen, D.R. Dekel, Water uptake study of anion exchange membranes, Macromolecules 51 (2018) 3264–3278, https://doi.org/10.1021/acs.macromol.8b00034.
[55] B. Kientiz, H. Yamada, N. Nonoyama, A.Z. Weber, Interfacial water transport effects in proton-exchange membranes, J. Fuel Cell Sci. Technol. 8 (2011), https://doi.org/10.1115/1.4002398.
[56] C.R. Wilke, C.Y. Lee, Estimation of diffusion coefficients for gases and vapors, Ind. Eng. Chem. 47 (1955) 1253–1257.
[57] Q. He, A. Kusoglu, I.T. Lucas, K. Clark, A.Z. Weber, R. Kostecki, Correlating humidity-dependent ionically conductive surface area with transport phenomena in proton-exchange membranes, J. Phys. Chem. B 115 (2011) 11650–11657, https://doi.org/10.1021/jp206154y.
[58] P. Sarkezi-Selsky, H. Schmies, A. Kube, A. Latz, T. Jahnke, Lattice Boltzmann simulation of liquid water transport in gas diffusion layers of proton exchange membrane fuel cells: parametric studies on capillary hysteresis, J. Power Sources 535 (2022), 231381, https://doi.org/10.1016/j.jpowsour.2022.231381.
[59] A. Thorell, L. Wadsö, Determination of external mass transfer coefficients in dynamic sorption (DVS) measurements, Dry. Technol. 36 (2018) 332–340, https://doi.org/10.1080/07373937.2017.1331239.
[60] R.K. Ahluwalia, X. Wang, W.B. Johnson, F. Berg, D. Kadylak, Performance of a cross-flow humidifier with a high flux water vapor transport membrane, J. Power Sources 291 (2015) 225–238, https://doi.org/10.1016/j.jpowsour.2015.05.013.
[61] X. Luo, S. Holdcroft, A. Mani, Y. Zhang, Z. Shi, Water, proton, and oxygen transport in high IEC, short side chain PFSA ionomer membranes: consequences of a frustrated network, Phys. Chem. Chem. Phys. 13 (2011) 18055–18062, https://doi.org/10.1039/c1cp22559f.
[62] G. Dorenbos, Y. Suga, Simulation of equivalent weight dependence of Nafion morphologies and predicted trends regarding water diffusion, J. Membr. Sci. 330 (2009) 5–20, https://doi.org/10.1016/j.memsci.2008.11.056.
[63] D. Wu, S.J. Paddison, J.A. Elliott, S.J. Hamrock, Mesoscale modeling of hydrated morphologies of 3m perfluorosulfonic acid-based fuel cell electrolytes, Langmuir 26 (2010) 14308–14315, https://doi.org/10.1021/la102358y.
[64] S. Cui, J. Liu, M.E. Selvan, S.J. Paddison, D.J. Keffer, B.J. Edwards, Comparison of the hydration and diffusion of protons in perfluorosulfonic acid membranes with molecular dynamics simulations, J. Phys. Chem. B 112 (2008) 13273–13284, https://doi.org/10.1021/jp8039803.
[65] A. Casalegno, F. Bresciani, G. Groppi, R. Marchesi, Flooding of the diffusion layer in a polymer electrolyte fuel cell : experimental and modelling analysis, J. Power Sources 196 (2011) 10632–10639, https://doi.org/10.1016/j.jpowsour.2011.08.094.
[66] M. Soniat, F.A. Houle, How the hydrophobic interface between a perfluorosulfonic acid polymer and water vapor controls membrane hydration, ACS Appl. Polym. Mater. (2021), https://doi.org/10.1021/acsapm.1c01805.
[67] G.S. Hwang, D.Y. Parkinson, A. Kusoglu, A.A. MacDowell, A.Z. Weber, Understanding water uptake and transport in Nafion using X-ray microtomography, ACS Macro Lett. 2 (2013) 288–291, https://doi.org/10.1021/mz300651a.